Hindawi
International Journal of Aerospace Engineering
Volume 2023, Article ID 1194655, 20 pages
https://doi.org/10.1155/2023/1194655

Research Article

Numerical Investigation of Aerodynamic and Electromagnetic Performances for S-Duct Caret Intake with Boundary-Layer Bleed System

Qiang Wang and Bin Wang

School of Energy and Power Engineering, Beihang University, Beijing 100191, China

Correspondence should be addressed to Bin Wang; jiji6611@163.com

Received 7 January 2023; Revised 13 April 2023; Accepted 19 April 2023; Published 5 May 2023

Academic Editor: Adel Ghenaiet

This study presents the numerical results for the aerodynamic and electromagnetic performances of an S-duct caret intake. Using the multilevel fast multipole method (MLFMM) to solve Maxwell equations, the current on the intake surface is calculated, and the radar cross-section (RCS) is analyzed. Moreover, the intake flow field is numerically investigated using the SST k–ω turbulence model to solve the Reynolds-averaged Navier–Stokes equations. Compared to a straight intake, for an S-duct caret intake, the average RCS is lower by 7.65 dB, and the maximum RCS difference value caused by the blade rotation is lower by 6.75 dB. However, the flow capacity deteriorates when the total pressure recovery coefficient decreases by 0.004. Based on the analysis of the aerodynamic and electromagnetic characteristics of different intakes, a double S-duct intake is designed. Compared to a traditional S-duct intake, for the novel intake after model parameter modification, the average RCS is lower by 0.05 dB, and the total pressure distortion (TPD) is lower by 0.18. The analysis of the effects of different boundary-layer bleed systems shows that the symmetrical layout adversely affects the aerodynamic and electromagnetic performances of the S-duct intake, but the unilateral partial layout is beneficial, whose TPD is lower by 0.04 and average RCS is higher by −2.17 dB compared to a straight intake.

1. Introduction

An advanced fighter aircraft should have not only excellent aerodynamic performance but also sufficient electromagnetic performance to cope with the increasingly complex electromagnetic detection environment. Due to the cavity configuration, the intake significantly influences the forward electromagnetic scattering characteristics of an aircraft [1]. Therefore, reducing the intensity of radar echo while ensuring the aerodynamic performance of the intake is particularly important when designing advanced fighter aircraft. Owing to its applicable aerodynamic performance [2] and electromagnetic performance, the caret intake has been widely used in various advanced aircraft.

Early studies generally evaluated the performance of intakes via experimentation [3–6]. With the development of computing technology, the aerodynamic performance of intakes is currently being efficiently analyzed using CFD [7]. Chaussee and Pulliam [8] used the diagonal form of the implicit approximate factor analysis algorithm to numerically simulate a two-dimensional, supersonic mixed-pressure intake with a Mach number of less than 2.0. To precisely investigate the complex viscous flow field with the secondary flow and flow separation, various turbulence models have been employed for numerically simulating S-duct intakes [9, 10]. Connolly et al. [11] applied the SST model to numerically analyze the principle of flow-separation in an S-duct intake. Furthermore, Gan and Zhang [12] used a

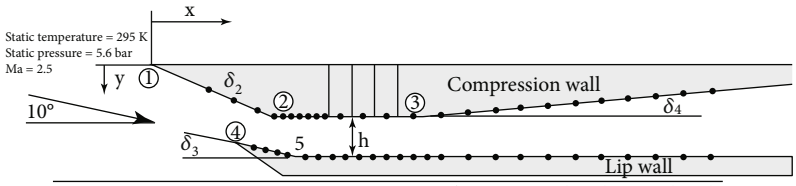

Parameters	Point coordinates	X (mm)	Y (mm)
Throat height h: 15 mm	1	0	0
Total length: 400 mm	2	45.7	18.0
Second compression angle δ_2: 21.5	3	75.0–145.0	18.0
Lip angle δ_3: 9.5	4	35.0	29.0
Expansion angle δ_4: 5	5	58.9	33.0

• Measurement point

Figure 1: Intake model and parameters.

modified k–ω turbulence model to optimize the model parameters of an S-duct diffuser, lowering the flow distortion by 16%.

In research on electromagnetics, the radar cross-section (RCS) value is usually used to measure the echo intensity of an object with the radiation of the electromagnetic wave. To precisely investigate the RCS value, various computational electromagnetic methods (CEMs) have been presented for calculating the surface current [13]. Umashankar et al. [14] used the method of moment (MOM) to analyze the RCS values of a simple cylinder composed of a low-scattering material and verified the usability of this method. Chung and Tuan [15] used the MLFMM to calculate and compare the RCS values of the S-duct and the straight intakes, showing that the S-bend diffuser could effectively improve the intake radar stealth performance.

Due to the short-distance configuration of S-duct diffusers, the secondary flow and boundary-layer separation universally exist in an S-duct intake, which worsens the aerodynamic performance [16, 17]. The boundary-layer bleed system is an effective method for suppressing this phenomenon and has been widely used in various intakes [18]. Furthermore, the interaction between the shock wave and boundary layer is universally present in the throat of supersonic intakes [19]. Huang et al. [20–23] used the boundary-layer bleed system to realize a secondary circulating jet for effectively suppressing this phenomenon. To improve the electromagnetic performance of an intake, two methods are effective: coating the duct with low-scattering materials [24] and connecting an S-duct diffuser to increase the reflected number of electromagnetic waves inside [25].

To date, studies on the caret intake have mainly focused on the design of the compression section, and studies considering an S-duct diffuser are relatively rare. Moreover, some independent research results of the aerodynamic and electromagnetic performances greatly limit the practical application of intakes. For example, the boundary-layer bleed system has been widely employed in intakes without any stealth requirement to improve the aerodynamic performance, but the effect of the system on the electromagnetic scattering performance has not been investigated. Therefore, during the research of S-duct caret intakes with a boundary-layer bleed system, the performances need to be comprehensively analyzed based on reliable CFD and computational electromagnetic methods.

2. Computational Methodology

The research scheme of this study was divided into five parts:

(1) The accuracies of the SST model for simulating the supersonic airflow and the MLFMM for the RCS calculation of cavity were verified via appropriate modeling using the commercial software Fluent 2022 and Feko 2020, respectively

(2) Mesh independency was studied using an S-duct caret intake with a Mach number of 2 and design altitude of 15 km under plane radar wave radiation of 3 GHz

(3) The defects and benefits of the S-duct diffuser were analyzed by comparing the performances of straight and S-duct intakes

(4) A new S-duct diffuser configuration with satisfactory performances was proposed by comparing the performances of four different design schemes

(5) The aerodynamic and electromagnetic performances of the intakes with different boundary-layer bleed systems were investigated

2.1. Method Verification. For the viscous flow simulation of an intake, a suitable turbulence model is essential for calculation accuracy [26]. Ou et al. [27] used multiple turbulence models to calculate and compare the simulation results of an S-duct intake and indicated that the SST model is the most precise in dealing with such complex flows. Therefore, the airflow of a mixed-compression intake was calculated using the SST model to verify the calculation precision [28]; the model and the parameters are shown in Figure 1.

The first-layer grid height was set as 0.0001 mm to ensure that y^+ was less than 1. A standard no-slip adiabatic wall was employed. Figure 2 presents the comparison between the calculation and experimental results of the compression and lip walls. In the figure, the y-axis is the ratio of

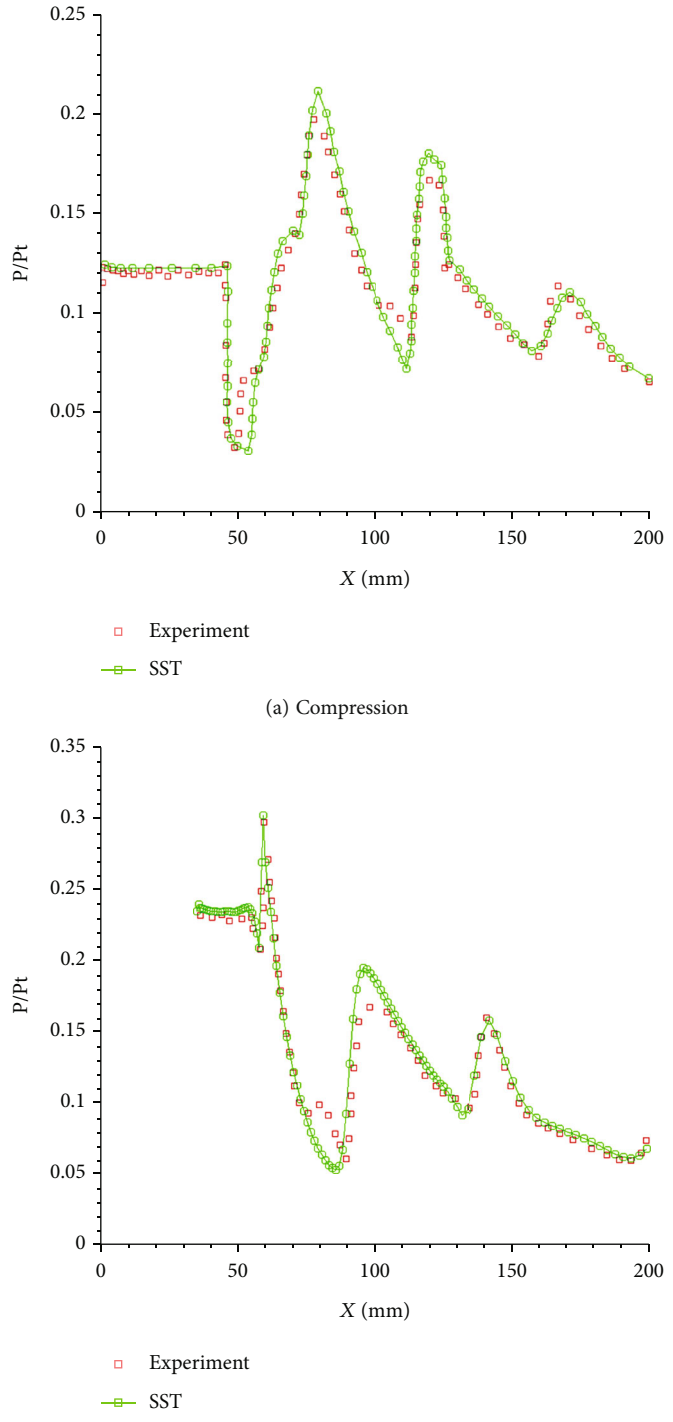

(a) Compression

(b) Lip

Figure 2: Wall pressure distribution.

the wall static pressure to the total pressure. Owing to the high consistency between the two results, the SST model was employed to numerically investigate the intake aerodynamic performance.

The RCS value of the cylindrical cavity was analyzed using multiple CEMs to test the accuracy [29]. The cavity model is shown in Figure 3. The methods included the physical optics (PO) method, ray launching-geometrical optics (RL-GO) method, MOM, and MLFMM. The incident wave was a plane electromagnetic wave with a frequency of 5 GHz. The angle between the incidence and model normal directions was varied from 0° and 50°, with intervals of 1°. The maximum mesh size was set as 0.75 mm. According to the results shown in Figure 4, the results calculated using

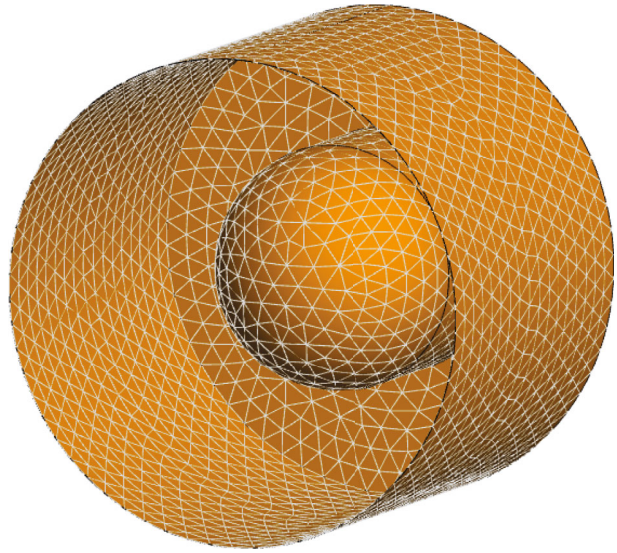

Figure 3: Model of the cylindrical cavity.

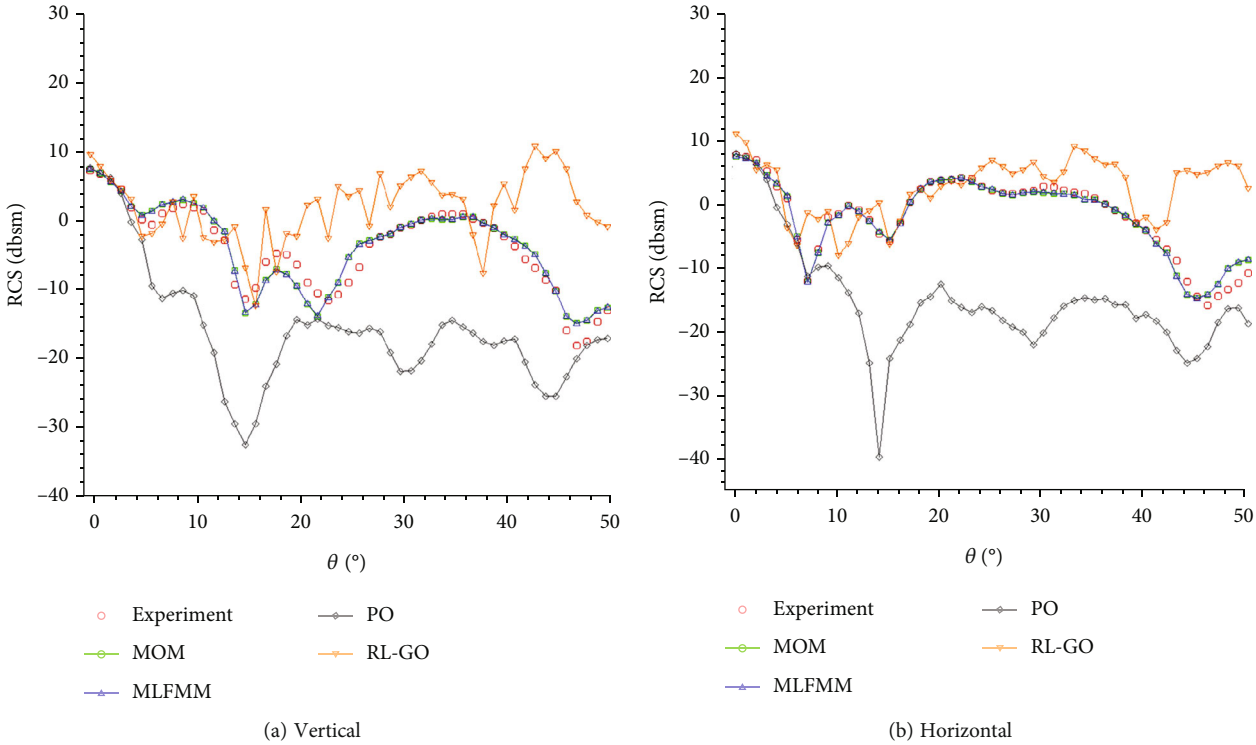

Figure 4: RCS results of the experiment and simulation with two polarizations.

MOM and MLFMM were more accurate than those calculated using the PO and RL-GO methods. Since the required memory of MLFMM is less than that of MOM, the MLFMM was utilized to calculate the intake RCS values.

2.2. Models and Boundary Conditions. To ensure that the engine was usable in the above described condition, an S-duct caret intake with an ideal flow of 80.55 kg/s was designed. The compression section parameters were calculated following the known design formula according to the outlet area and flight condition. Based on the design condition, an oblique shock wave at the inlet and a positive shock wave at the throat formed at the compression section of the caret intake. According to the gas parameter formula around the oblique and positive shock waves, the optimal oblique shock angle to achieve minimum total

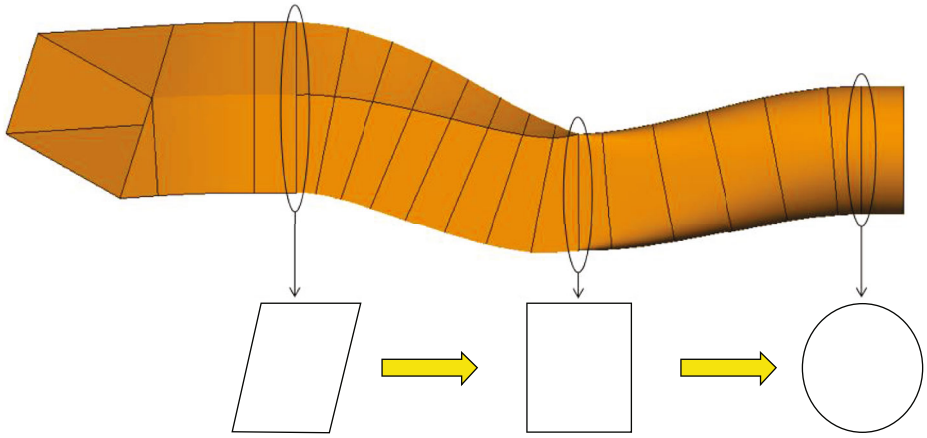

	Length (m)
Total	6.5
Throat	0.4
Front diffuser	2
Rear diffuser	2
Straight section	0.3
	Area (m^2)
Inlet	0.709
Throat	0.502
Outlet	0.636

(a) Intake model and parameters

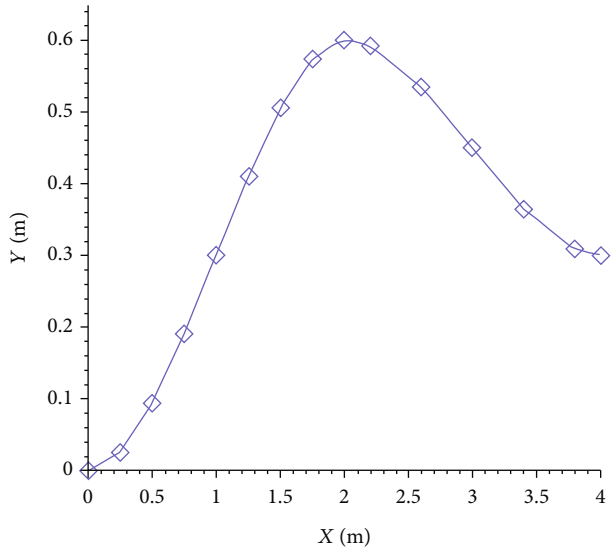

(b) Center coordinates of the diffuser sections

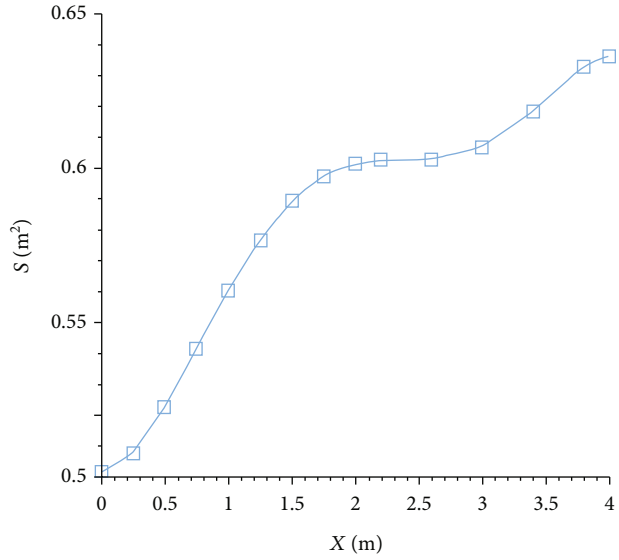

(c) Areas of the diffuser sections

Figure 5: Model and parameters of the caret intake.

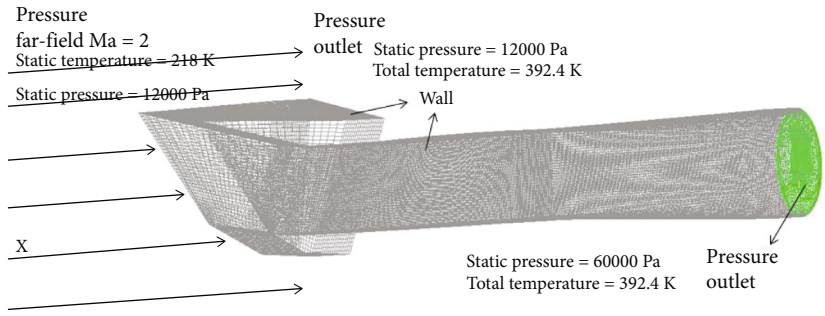

Figure 6: Mesh and boundary conditions for flow field calculations.

pressure loss was determined as 45.7°. The inlet area can be determined using the flow formula according to the design flow and far field gas conditions, and the inlet length is usually determined using the aircraft parameters to match the intake with the aircraft. For the front diffuser, the center point of the diffuser inlet was taken as the origin of coordinates.

Assume:

$$X_n = \frac{x_n}{x_8},$$
$$Y_n = \frac{y_n - y_0}{y_8 - y_0}. \quad (1)$$

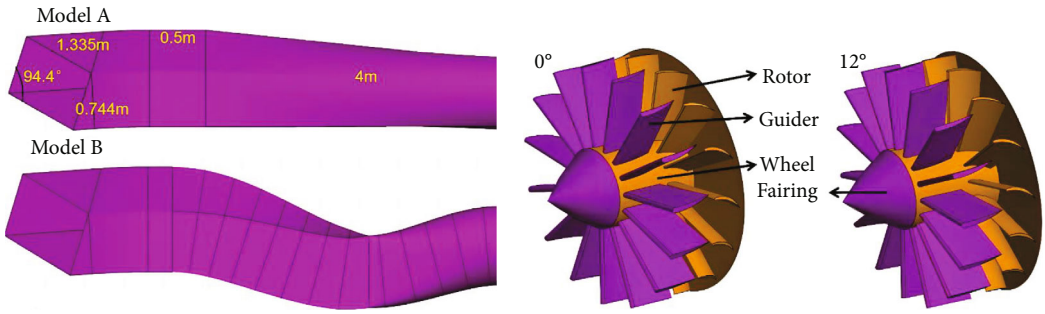

(a) Models of two intakes (b) Models of compressors with two rotation angles

Figure 7: Numerical calculation models for the electromagnetic characteristics.

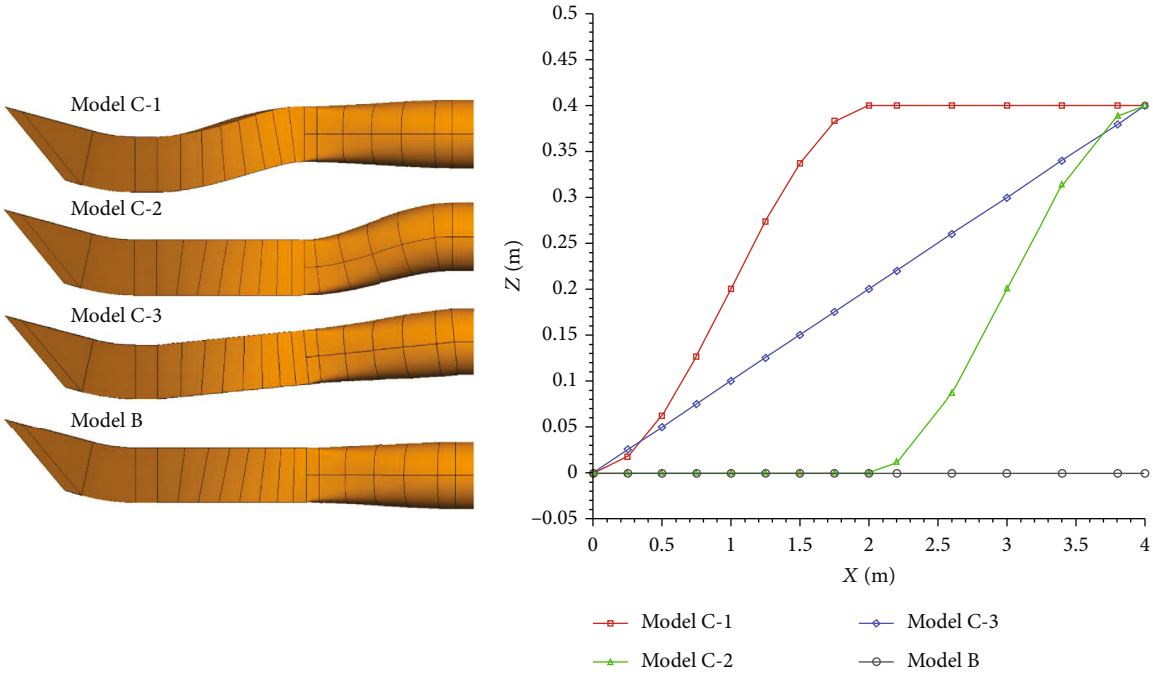

(a) Models of intakes (b) Center coordinates of diffuser sections

Figure 8: Models and parameters of the intakes with the outlet biased in two directions.

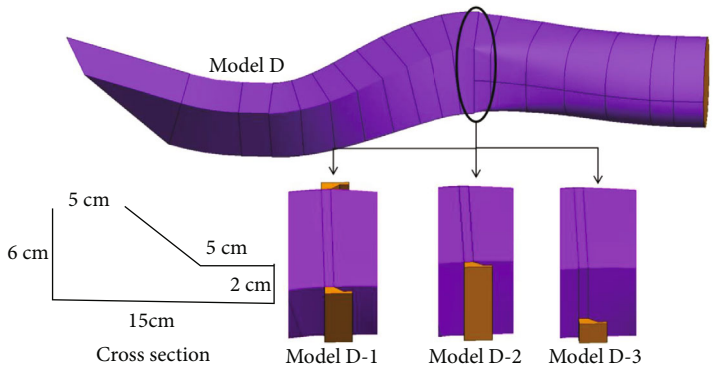

Figure 9: Models of the different boundary-layer bleed systems.

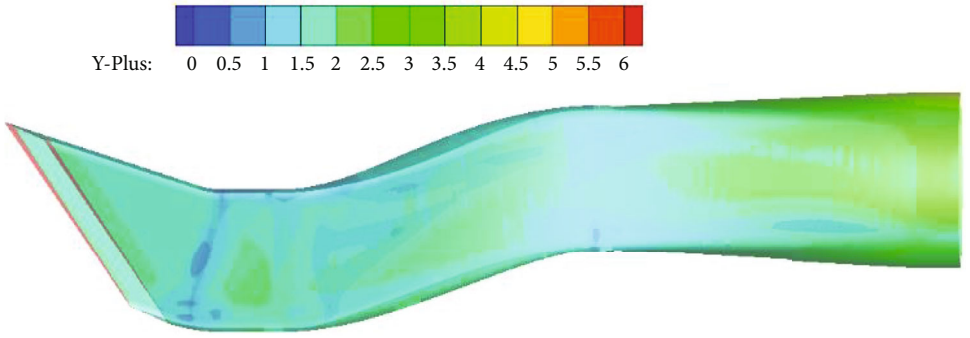

(a) Y-plus of the inner wall

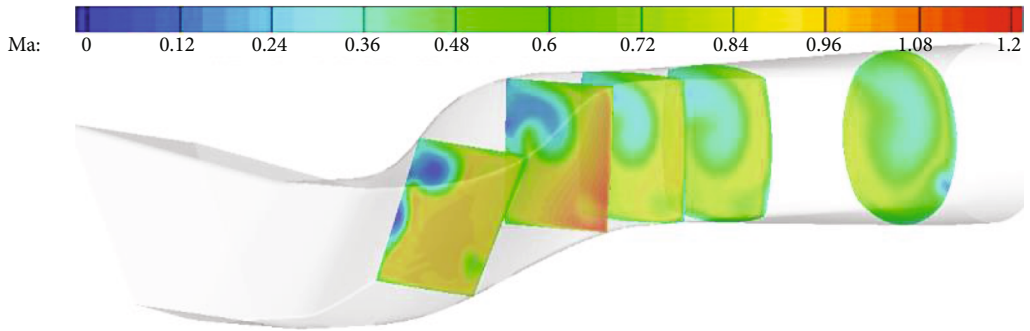

(b) Mach number distribution with A-mesh-D

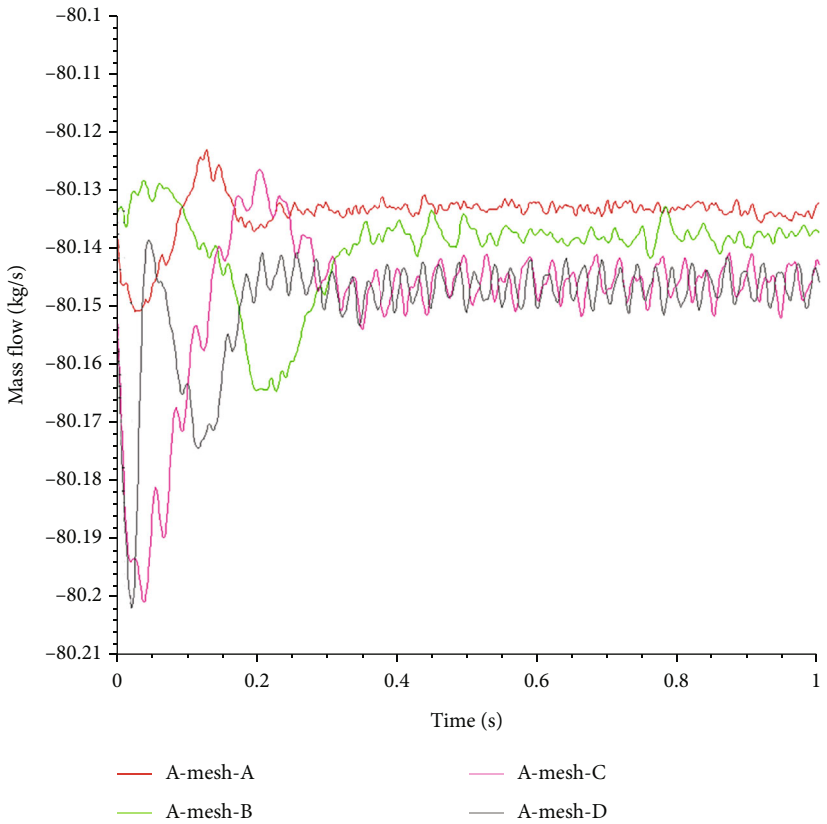

(c) Mass flow rate variations at the outlet

Figure 10: Continued.

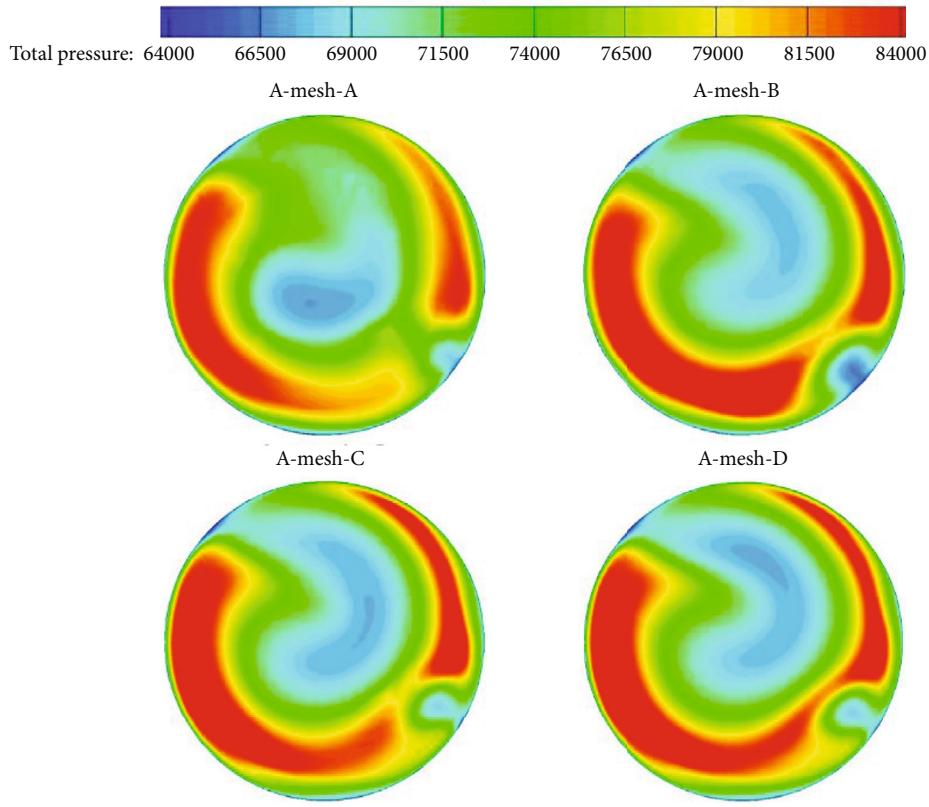

(d) Total pressure distribution of the outlet

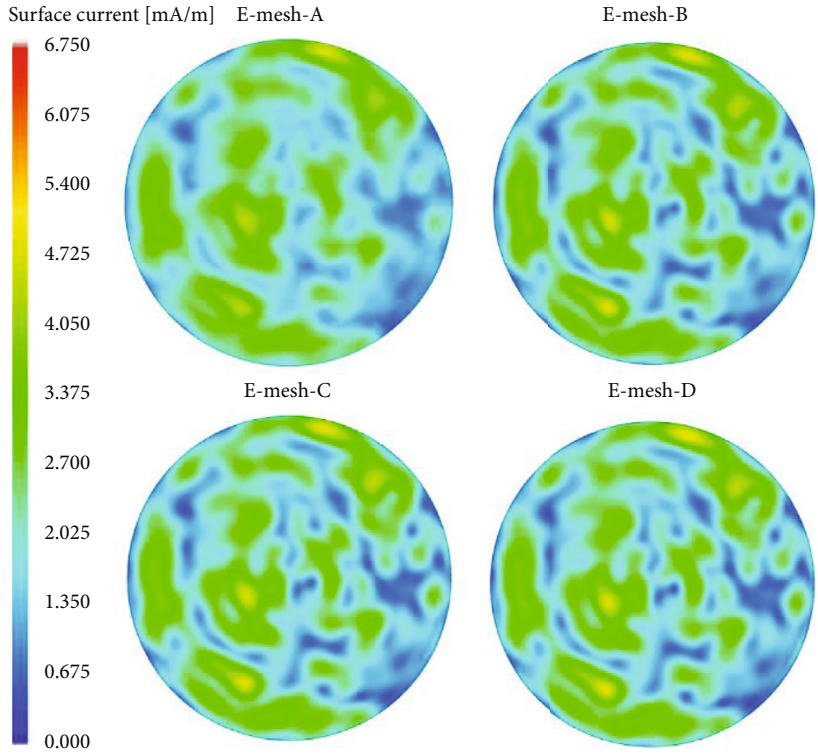

(e) Surface current distribution of the outlet

Figure 10: Y-plus of inner wall and parameter distributions of the outlet.

Table 1: Mesh type and performance parameters.

Aerodynamic performance					Electromagnetic performance			
Mesh type (A-mesh-)	Mesh number (million) Inner	Whole	Flow (kg/s)	Average total pressure (Pa)	Mesh type (E-mesh-)	Mesh size	Mesh number (million)	RCS (dBsm)
A	0.54	0.83	80.133	76811.5	A	$\lambda/4$	0.26	3.95
B	1.02	1.33	80.138	77088.2	B	$\lambda/6$	0.71	3.37
C	1.98	2.41	80.145	77203.9	C	$\lambda/8$	1.02	3.13
D	3.15	3.69	80.146	77228.8	D	$\lambda/10$	1.59	3.11

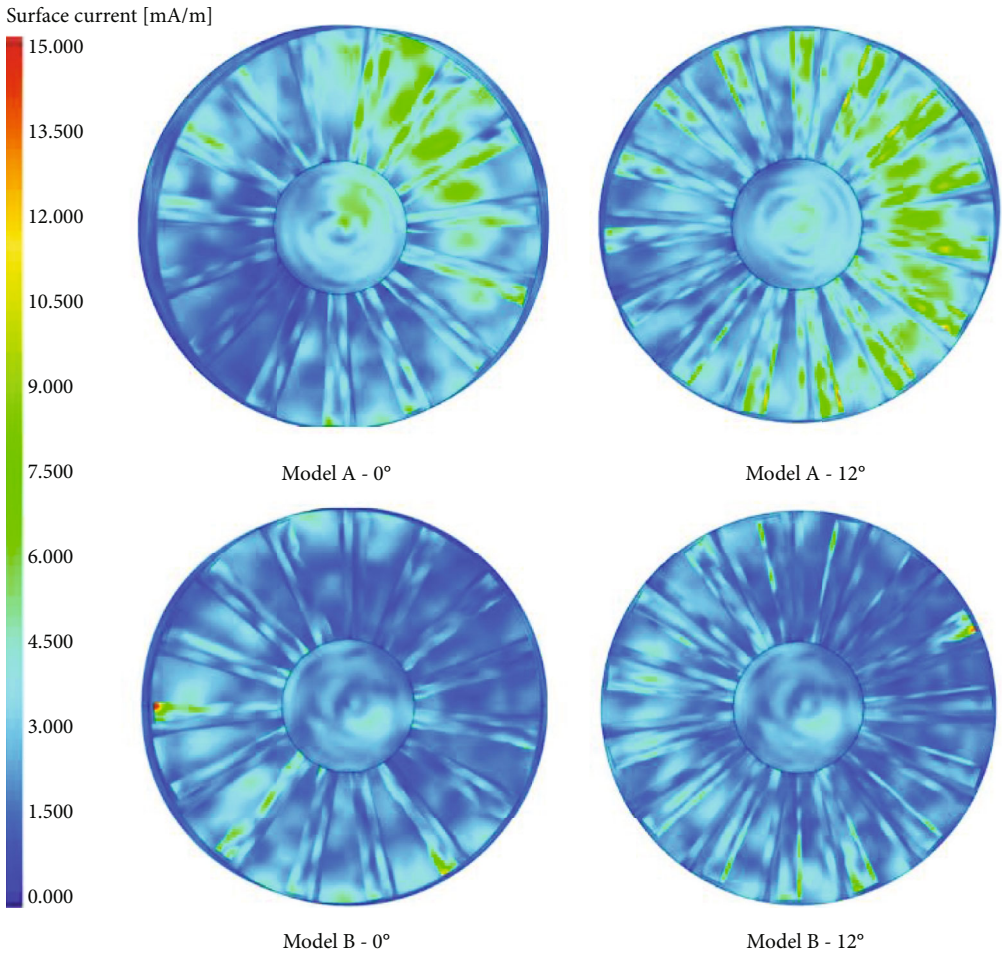

Figure 11: Surface current distribution of the blades and outlet.

The x_n is the x-axis coordinate of the n-th section center. The y_n is the Y-coordinate of the n-th section center. The 0th and 8th sections represent the inlet and outlet of the front diffuser, respectively. Four conditions were determined to ensure the continuity of diffuser inlet and outlet parameters: when $X = 0$, $Y = 0$, and $\dot{Y} = 0$ and when $X = 1$, $Y = 1$, and $\dot{Y} = 0$.

Therefore, by using the quartic polynomial functions, the variation of all model parameters could be expressed as

$$Y = AX^4 + BX^3 + CX^2 + DX + E, \quad (2)$$

substituting the four conditions into the following equation:

$$Y = AX^4 - (2 + 2A)X^3 + (3 + A)X^2. \quad (3)$$

The value of parameter A ranges from -3 to 3. The six-sectioned center coordinates of the rear diffuser were determined by using the similar method, and the section areas of the entire diffuser were also determined by using a sixth-degree polynomial function after ensuring the continuity of the area around the middle section.

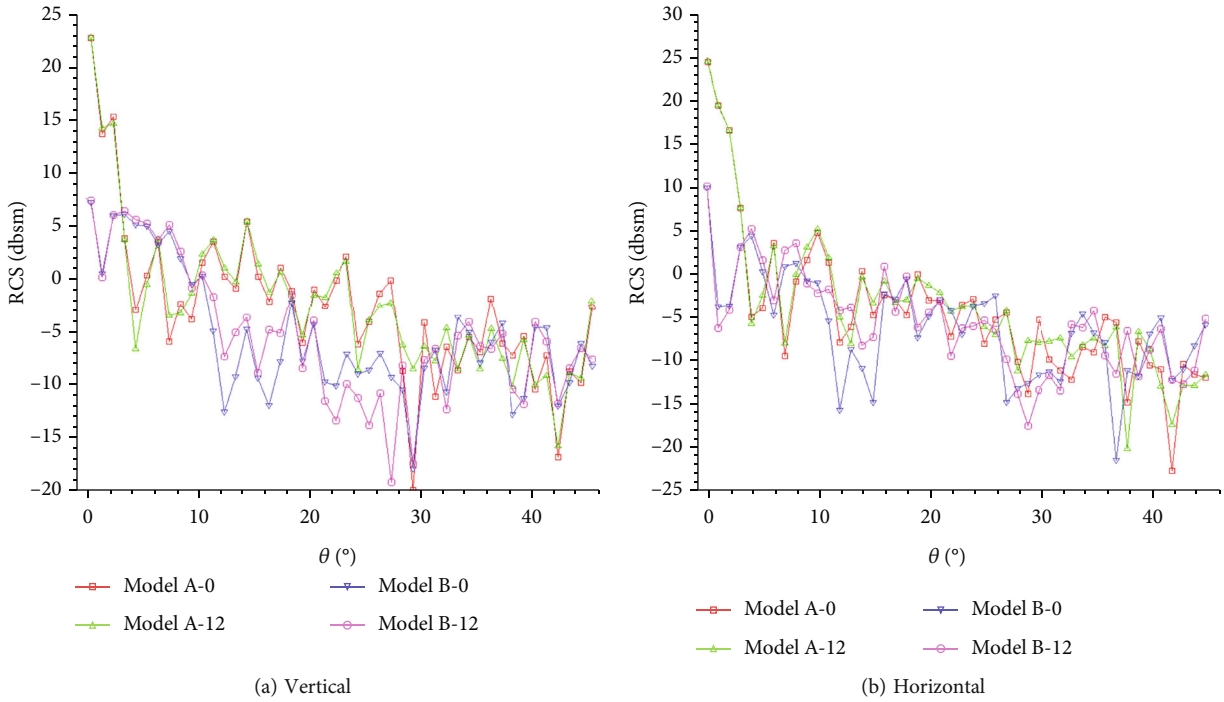

Figure 12: RCS values of the different intakes with two polarizations.

Table 2: Electromagnetic scattering and aerodynamic characteristics of the intakes.

Polarization	RCS (dBsm)	Model A		Model B	
		0°	12°	0°	12°
Vertical	Average	8.24	8.28	−0.70	−0.39
	Maximum	23.24	23.31	7.65	7.80
	Maximum difference	5.61		−3.42	
Horizontal	Average	10.54	10.58	−1.34	−0.83
	Maximum	25.14	25.23	10.67	10.78
	Maximum difference	7.67		0.47	
Outlet pressure (Pa)		60,000	65,000	60,000	
Flow coefficient		0.9962	0.9959	0.9934	
TPR coefficient		0.8349	0.8646	0.8310	
Distortion index DC60		0.4515	0.4483	0.3621	

The model and parameters are shown in Figure 5, and all the polynomial parameters were set as 0. To ensure that the radar stealth characteristics of the aircraft and intake matched, the inlet of the caret intake was designed as a parallelogram. The shape of the cross-section changed from a parallelogram to a rectangle in the front diffuser and to a circle in the rear diffuser. The boundary conditions used for the flow field calculation are shown in Figure 6.

The caret intake is usually installed inside the fuselage of an aircraft. To accurately analyze and compare the RCS values of different intakes, a uniform cavity was designed to wrap each intake. To effectively suppress the echo intensity, the walls of the cavity and intake were coated with a low-scattering material whose relative magnetic permeability $\mu_r = 1.29 - 0.57j$ and relative dielectric constant $\varepsilon_r = 9.72 - 1.08j$. The intake outlet was set as an ideal electrical conductor. A plane wave with a frequency of 3 GHz was employed as the electromagnetic wave. The XOY plane was defined as the horizontal plane. The angle between the x-axis and the incident direction was varied from 0° to 45° with intervals of 1°, parallel to the horizontal plane.

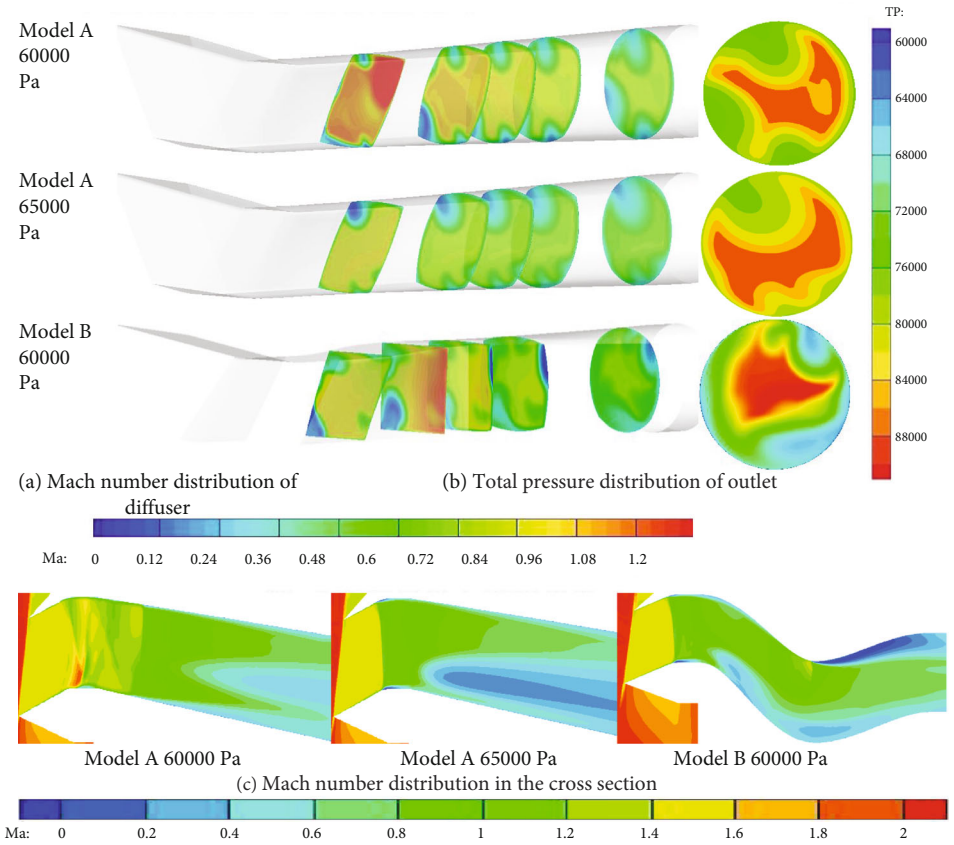

Figure 13: Results of the intake flow field calculation with different conditions.

First, the electromagnetic and aerodynamic performances of two intakes with different diffusers were evaluated: model A (a straight intake) and model B (an S-duct intake). To analyze the effect of blade rotation on the electromagnetic performance, the outlets of the two intakes were connected to two compressors with different rotation angles of the rotor blades, as shown in Figure 7. The rotation angle of one rotor was set as 0°, while that of the other was set as 12°, which is half of the angle between the two blades. The height and width of the blades were 0.3 and 0.15 m, respectively. The speed of the blade rotation was far less than that of an electromagnetic wave, and the influence of the rotation speed on the echo intensity was ignored. The materials of the rotor blade and wheel were ideal electric conductors. The surfaces of the guide vanes and fairing were coated with a low-scattering material. The model outlet was set as an ideal electric conductor. The boundary conditions for the electromagnetic scattering calculation were the same as those described above.

Then, four different S-duct intakes with the outlet biased in two directions were considered, as shown in Figure 8(a). The parameters of each model were roughly identical, except for the center Z-coordinates of the diffuser sections, as shown in Figure 8(b). The coordinates of model C-1 were varied in the front diffuser, and those of model C-2 were varied in the rear diffuser, with the quartic polynomial parameters of 0. The coordinates of model C-3 were linearly varied throughout the diffuser. The boundary conditions of the numerical calculation were the same as those described above, and the influence of the blade rotation was ignored.

As has been proven, the boundary-layer bleed system can effectively improve the aerodynamic performance of an intake, but its effect on the electromagnetic performance is still unknown. After changing the polynomial parameter of the sectional area to 1.5, a new intake named model D with a small DC60 value was established. To investigate the effect of the BL bleed system, three different systems were installed in the middle section, as shown in Figure 9: a symmetrical layout named model D-1, a unilateral layout named model D-2, and a unilateral partial layout named model D-3. The height of model D-3 was one-third that of model D-2. All the surfaces of the systems were ideal electric conductors.

2.3. Mesh Dependency Study. The mesh quantity and quality play an important role on the flow and the current numerical investigation. To determine the most suitable mesh number, four kinds of meshes were generated during the mesh-dependence study. MLFMM based on the sparse approximate inverse preconditioner was used to determine the RCS values of the intake radiated by a vertically polarized radar wave with an incident angle of 0°. The calculation was stopped at the residuum of 0.01. Using the structured mesh, the flow field was calculated by coupling the mass,

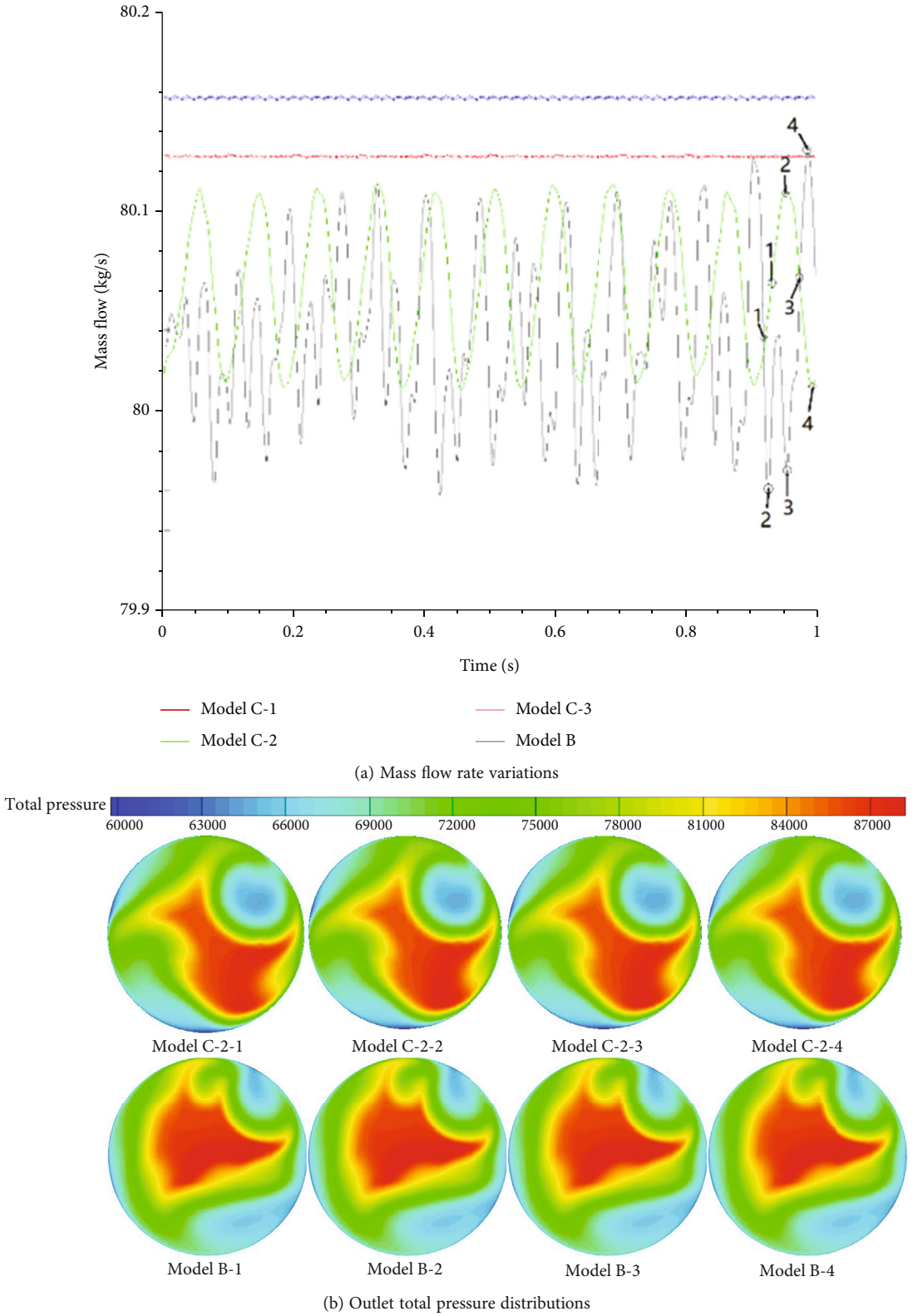

(a) Mass flow rate variations

(b) Outlet total pressure distributions

Figure 14: Results of the flow field calculated by the transient method.

momentum, and energy equations with the steady-density-based formulation. The minimum height of the near-wall grid was set as 0.02 mm to ensure that the wall Y-plus was between 0 and 10. The sum of all the flows at the inlets and outlet was defined as the detection flow. The calculation was stopped after the detection flow was stably less than

Table 3: Outlet aerodynamic parameters of models C-2 and B.

Model		Mass flow rate (kg/s)	Total pressure (Pa)		
			Average	Maximum	Minimum
C-2	Average	80.0417	78,009.32	88,431.31	60,338.26
	Point 1	80.0426	77,995.37	88,414.78	60,335.34
	Point 4	79.9908	77,999.46	88,512.37	60,333.56
B	Average	80.0168	78,024.47	88,953.46	61,123.32
	Point 1	80.0149	78,028.89	88,989.35	61,115.43
	Point 4	80.1129	77,991.93	88,861.60	61,135.39

0.01 kg/s, with the residuals of k and continuity of less than 0.001. Furthermore, to analyze the effect of the mesh number, the transient method was used to calculate the variation of the mass flow rate based on the same turbulence model. The calculation time was set as 1 s with a time step of 0.001 s, and each step was iterated 15 times. Figure 10 depicts the Y-plus of the intake inner wall and the results of the flow field calculations. The number of each mesh and multiple mesh parameters are presented in Table 1. Comparison showed that the total pressure distribution of the outlet and performance parameters significantly changed when the total mesh number exceeded 2.4 million and the inner mesh number exceeded 1.98 million. The same conclusion was observed when the outlet mass flow was varied with time. The critical mesh number was set as 1.02 million in the electromagnetic simulation. Therefore, the mesh numbers for the two intakes were set as 2.4 million and 1.02 million.

3. Results and Discussion

3.1. Effect of S-Duct Diffuser. Figure 11 depicts the surface current distributions of the blades and outlets of different intakes irradiated by a horizontally polarized electromagnetic wave with an incident angle of 0°. Due to the direct radiation of the electromagnetic wave, the surface currents on the right side were significantly greater than those on the left side at the outlet of the straight intake. Due to the shielding of the rectifier blades, the surface currents of the rotor blades with the phase angle of 0° were significantly smaller than those of the model with the phase angle of 12°. In addition, a partial electromagnetic wave was reflected from the rotor blades with the phase angle of 12° to the outlet, which significantly increased the area of the large-current zone on the outlet surface. Due to the absorption of the low-scattering material, the electromagnetic wave was repeatedly reflected between the walls of the S-duct intake and became weak, before irradiating the outlet, resulting in smaller surface currents and a less significant effect of blade rotation compared to the straight intake.

Figure 12 presents the RCS values for the four intakes, and the two performance parameters are illustrated in Table 2. The flow coefficient is the ratio of the actual flow rate at the outlet to the ideal flow rate, which was 80.55 kg/s, and the total pressure recovery (TPR) coefficient is the ratio of the average total pressure at the outlet to the outflow total pressure, which was 93,893 Pa. The distortion index DC60 was calculated using the following equation:

$$\mathrm{DC60} = \frac{\bar{P}^* - \bar{P}^*_{\min}(60)}{\bar{q}}, \tag{4}$$

where $\bar{P}^*_{\min}(60)$ is the minimum average total pressure of the sector with an angle of 60° at the outlet and $\bar{q}$ is the average dynamic pressure of the outlet.

The results showed that the effect of the rotor blade rotation was generally less pronounced in the S-duct intake than in the straight intake. The RCS values of the S-duct intake were considerably smaller than those of the straight intake with an incident angle of 0°–3° and were steadily less than 0 dB with an incident angle of 10°–45°. Therefore, the maximum and average RCS values of the S-duct intake were lower than those of the straight intake after each polarization. In addition, the RCS differences of the S-duct intake caused by the blade rotation were effectively stable below 0.5 dB. Thus, the calculation model can be simplified by ignoring the influence of the blade rotation.

The flow field calculation results are shown in Figure 13. As shown in the figure, the internal flow at the first section of the straight intake comprises an obvious supersonic zone with an outlet pressure of 60,000 Pa, which disappeared with an outlet pressure of 65,000 Pa, meaning that the intake remained subcritical until the outlet pressure reached 65,000 Pa. In contrast, the S-duct intake was at the critical state with the outlet pressure of 60,000 Pa due to its worse actual flow capacity. In conclusion, the ability to withstand the change in outlet pressure decreased after connecting the S-duct diffuser.

In addition, only one low-speed zone was present around the upper left of the diffuser in the straight intake with an outlet pressure of 65,000 Pa, which stemmed from the irregular change in the section shape. Naturally, a large low-pressure area appeared at the upper left of the outlet section. In contrast, the curved pipeline of the S-duct diffuser led to a more complicated flow distribution. At one side of the second section, the internal flow was pushed by the wall, which accelerated it, forming a local supersonic zone in the S-duct intake. Correspondingly, a low-speed zone formed on the other side. The supersonic zone eventually formed a local shock wave in the middle section of the diffuser. The interaction between the shock wave and the boundary layer downstream resulted in a low-speed zone. Finally, only a small high-pressure zone was present at the outlet. Furthermore, due to the local shock wave and the mixing of the low- and high-speed airflows in the S-duct intake, the TPR coefficient decreased by approximately 0.357. However, the low-pressure zone in the outlet section of the straight intake was more concentrated than that in the S-duct intake, yielding a relatively higher DC60 coefficient of 0.1121.

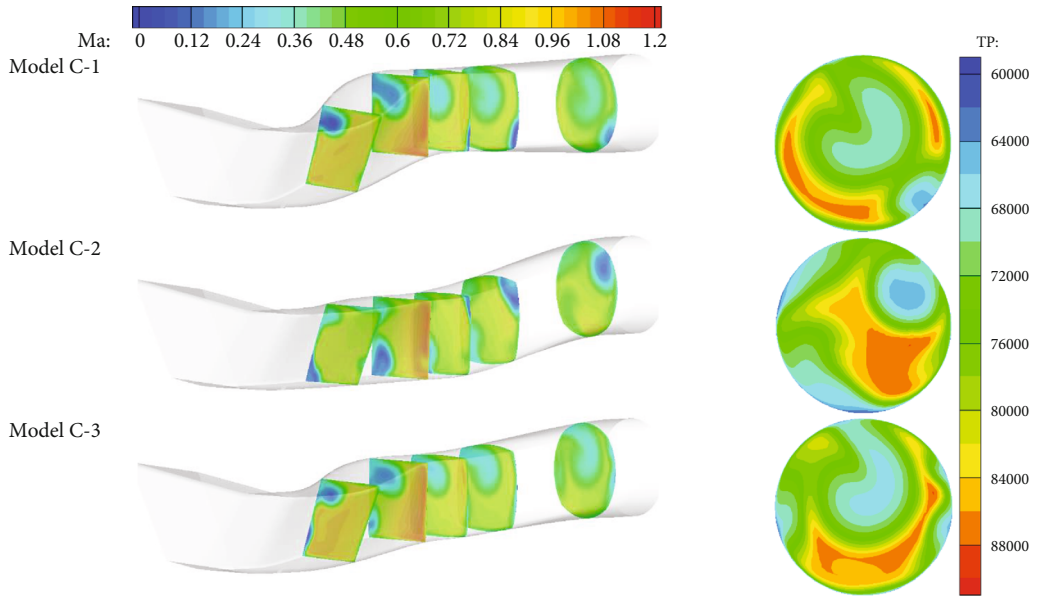

Figure 15: Flow field calculation results of the different intakes.

Table 4: Aerodynamic parameters of the four intakes.

	Model C-1	Model C-2	Model C-3	Model B
Flow coefficient	0.9945	0.9937	0.9948	0.9934
TPR coefficient	0.8204	0.8307	0.8235	0.8310
Distortion index DC60	0.2899	0.4591	0.3381	0.3621

3.2. Aerodynamic Characteristics of S-Duct Caret Intake. Based on the above results, backflow may occur in the S-bend diffuser, resulting in the instability of the outlet parameters during the calculation. To more comprehensively investigate the aerodynamic characteristics, the transient method was used for calculation based on the calculation results of the steady method, with a time step size of 0.001 s and total time of 1 s. The variations of the mass flow rate at the outlets of the four intakes are shown in Figure 14(a). In contrast to models C-1 and C-3, the mass flow rates of models C-2 and B greatly varied with the computation time, signifying the occurrence of backflow. However, the parameters of model B varied more complexly than those of model C-2; thus, more backflow zones were present in model B than in model C-2. The outlet total pressure distributions of the models C-2 and B at four respective points marked in Figure 14(a) are shown in Figure 14(b). Despite the different mass flow rates, the total outlet pressure distributions of model C-2 at these four points were almost the same, similar with model B.

Table 3 presents the four aerodynamic parameters at the outlets of models C-2 and B, including the average value of all results and the transient results at the two points. The sum of all the outlet mass flow rates was almost similar to the sum of the inlet mass flow rates at point 1 and was the most different from that at point 4. The differences of all the parameters between the average value and the value at point 1 were almost negligible, indicating that no overflow occurred at the inlet during the calculations. Therefore, the outlet parameter variations were only related to the backflow, with no effect on the shock wave at the inlet. Combined with the above analysis of the outlet total pressure distribution, to some extent, the average performances can be replaced by the transient performances of the intake at point 1.

The flow field calculation results for the different intakes are shown in Figure 15, and the three aerodynamic parameters are presented in Table 4. The results of models C-2 and B are the calculation results at point 1. Notably, the change of the diffuser centerline led to an increase of the low-speed area and even boundary-layer separation in some cases. Comparison showed that the change to this model parameter had little influence on the airflow capacity in the critical state but had a prominent influence on the outlet total pressure distribution. Compared to the other models, the parameters of model C-1 mainly changed in the front diffuser, resulting in an uneven airflow distribution for the low-speed and supersonic zones. However, the airflow could be stably mixed in the rear diffuser, thus creating a regular distribution at the outlet. Accordingly, the DC60 value of model C-1 increased to 0.2899, and the TPR coefficient decreased to 0.8204 as a cost.

3.3. Electromagnetic Characteristics of S-Duct Caret Intake. In terms of the electromagnetic scattering characteristics, a new index named "safety angle" (SA) was established; the RCS value was less than 0 dB at this incident angle. The greater the SA, the more working conditions the intake can be applied to. The RCS simulation results are shown in

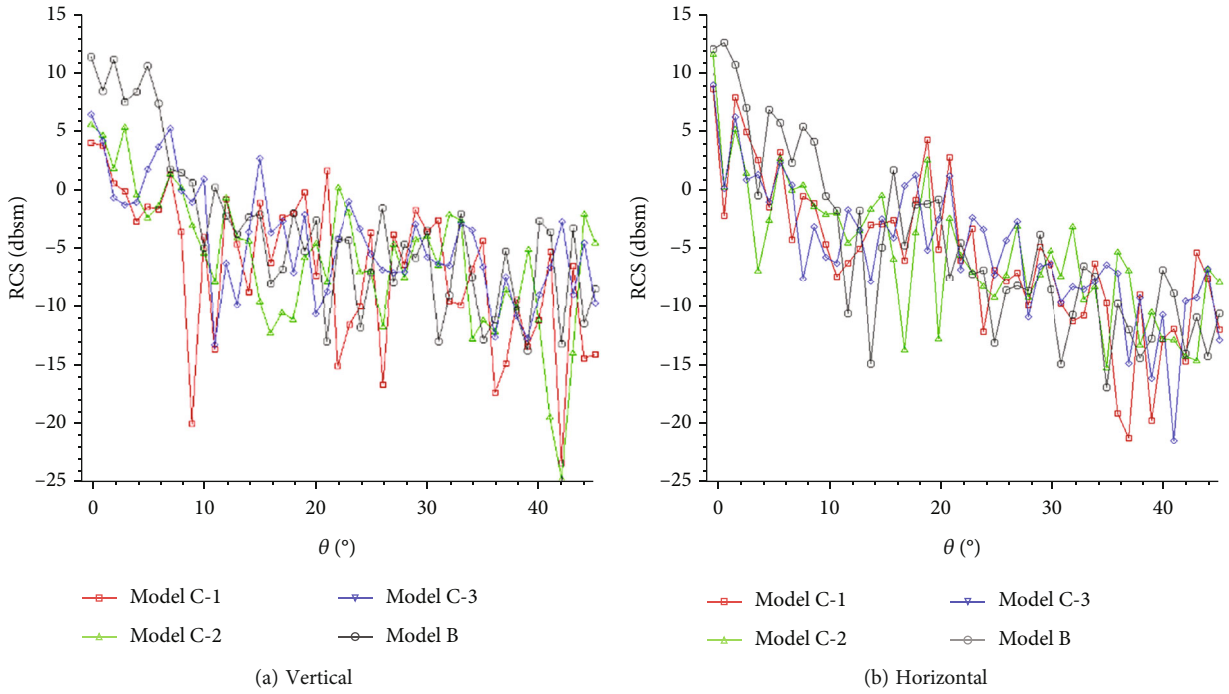

Figure 16: RCS values of the different intakes with two polarizations.

Table 5: Electromagnetic parameters of the four intakes.

Polarization	RCS (dBsm)	Model C-1	Model C-2	Model C-3	Model B
Vertical	Average	−3.26	−2.45	−1.76	2.26
	Maximum	3.95	5.49	6.36	11.29
	Numbers of SA	41	39	39	34
Horizontal	Average	−0.84	−0.76	−1.32	2.49
	Maximum	8.79	11.72	9.12	12.71
	Numbers of SA	39	38	36	35

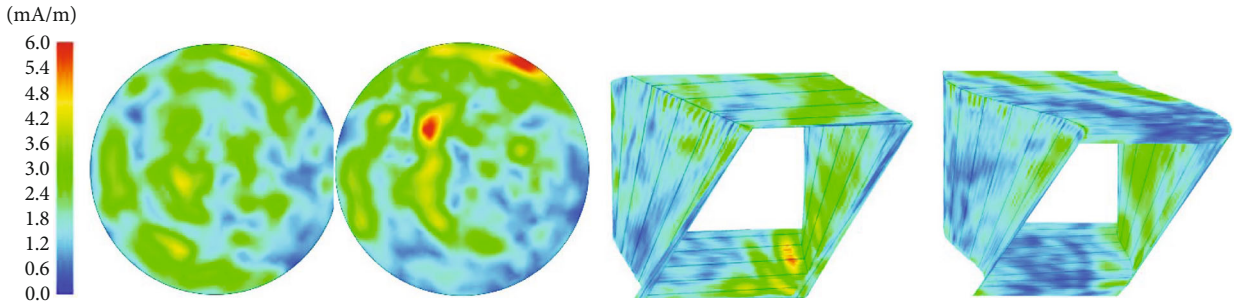

Figure 17: Surface current distribution of the outlet and front diffuser.

Figure 16, and the three electromagnetic parameters are presented in Table 5. Comparison showed that each index of the three intakes with the outlet biased in two directions was better than that of the traditional S-duct intake, proving that the proposed design scheme can effectively improve the electromagnetic performance of the intake. As the bias direction increased, the area of the outlet section directly exposed to radiation decreased with minor incident angles. Therefore, the RCS values of model B were significantly greater than those of the other models with incident angles of 0°–10°.

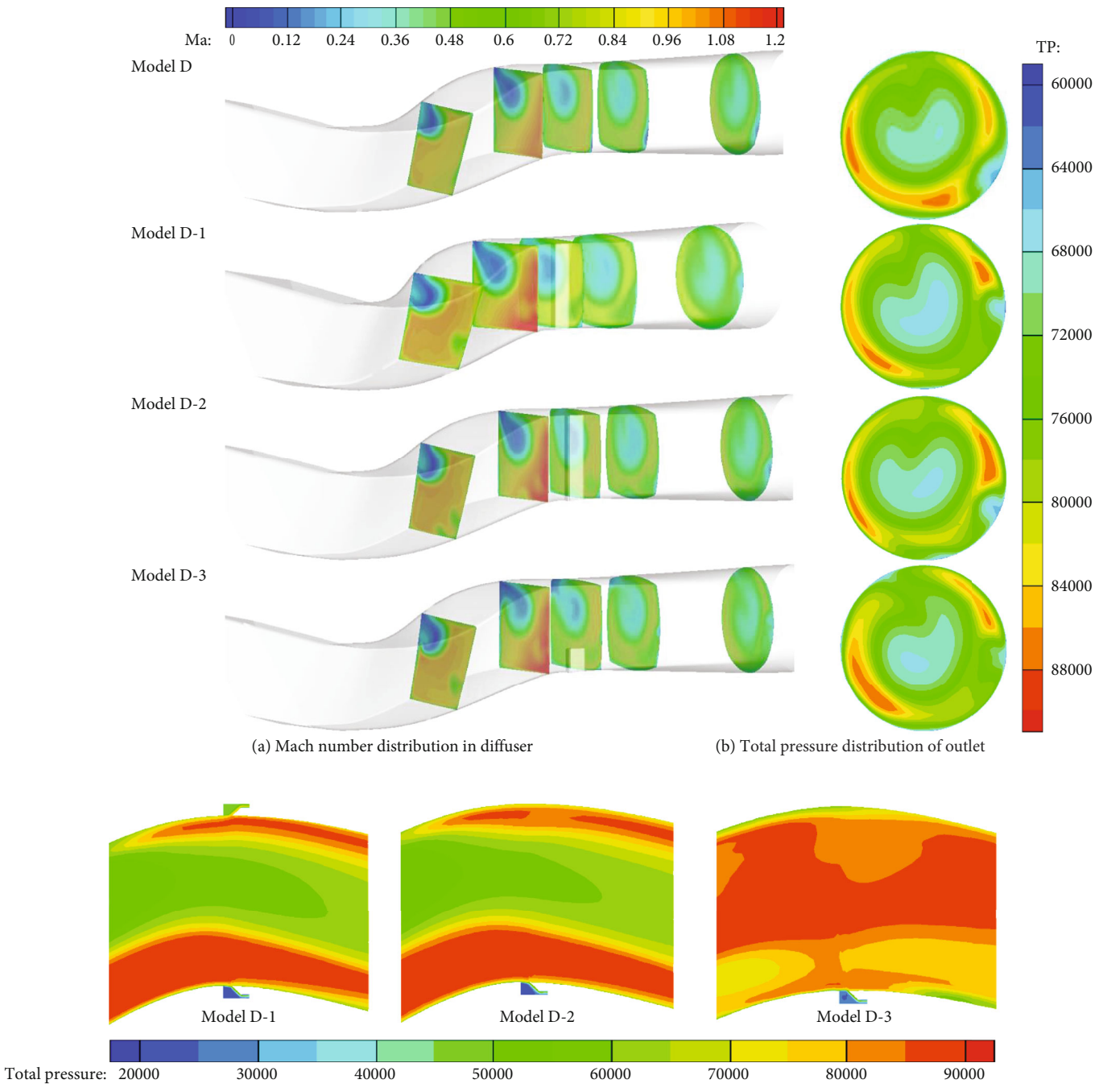

(a) Mach number distribution in diffuser

(b) Total pressure distribution of outlet

(c) Total pressure distribution of the boundary-layer bleed system

Figure 18: Flow field calculation results of the different intakes.

When the incident angle was varied from 10° to 45°, the RCS values of the four models remained stable at a low level and met the design requirements.

Figure 17 shows the partial current distribution of two intakes radiated by a vertically polarized wave with an incident angle of 0°. The outlet surface currents of model C-1 were obviously smaller than those of model C-2, indicating that the variation of parameters such as in model C-3 made the shielding of the wall more effective. However, a large-current zone appeared in the front diffuser, which is obviously detrimental to the performance of model C-1. The currents in this zone exceeded those of the outlet, representing a substantial change in the main electromagnetic scattering sources of the intake.

In conclusion, by connecting a diffuser in a similar way to that in model C-1, the electromagnetic scattering performance and the outlet total pressure distribution of the intake can be improved without affecting the flow rate. However, this design inevitably leads to an increase in the total pressure loss and the electromagnetic scattering sources of the intake. Therefore, further modifications of the model parameters and relevant improvement measures are necessary.

Table 6: Electromagnetic scattering and aerodynamic characteristics of the intakes.

Polarization	RCS (dBsm)	Model D	Model D-1	Model D-2	Model D-3
Vertical	Average	−1.33	−0.20	−0.33	−1.29
	Maximum	5.88	4.83	6.03	5.41
	Numbers of SA	37	31	33	36
Horizontal	Average	−1.17	−0.85	−1.34	−1.45
	Maximum	7.30	8.54	7.54	6.98
	Numbers of SA	36	39	37	37
Flow coefficient		0.9942	0.9635	0.9819	0.9923
TPR coefficient		0.8185	0.8078	0.8126	0.8154
Distortion index DC60		0.1847	0.1714	0.1243	0.1461
Boundary-layer bleed system outlet	Mass flow (kg/s)		2.64	1.01	0.25
	Average total pressure (Pa)		52,119	39,960	33,858

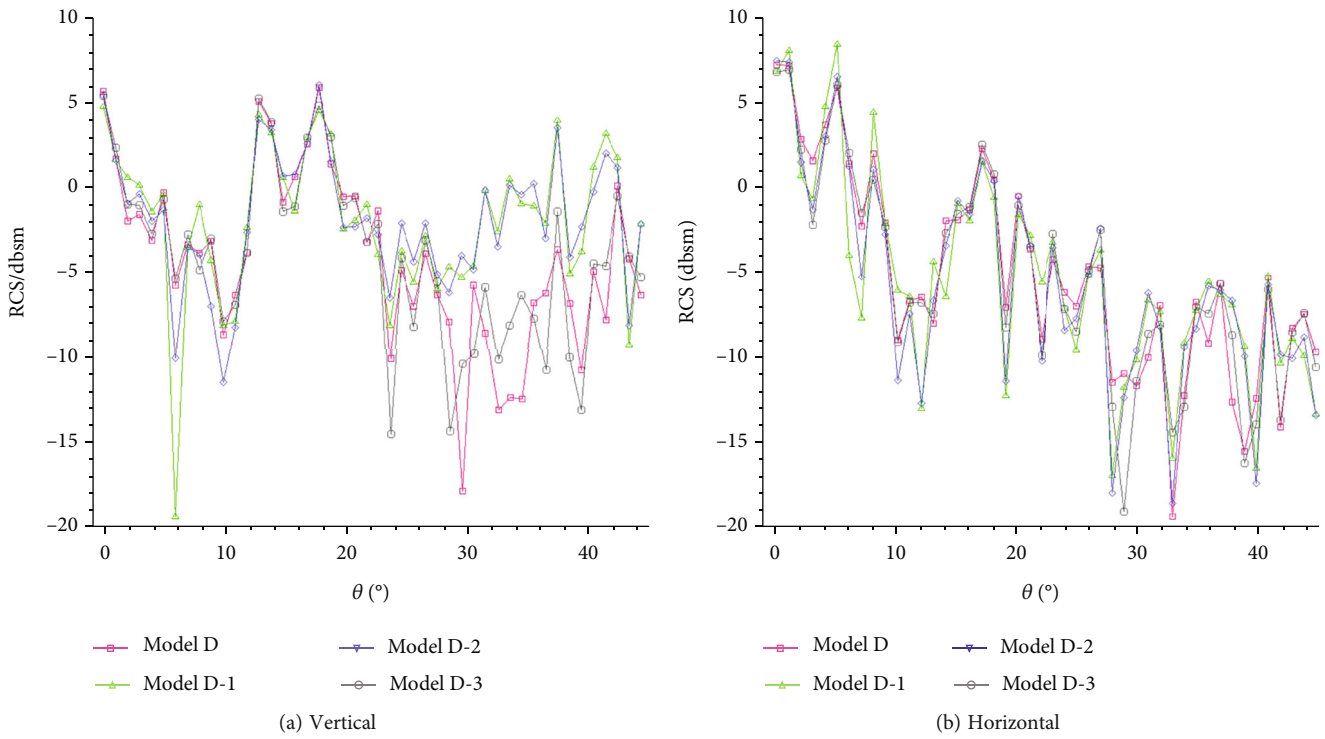

(a) Vertical (b) Horizontal

Figure 19: RCS values of the different intakes with two polarizations.

3.4. Effect of Boundary-Layer Bleed System. The flow field calculation results for different intakes are shown in Figure 18, and the parameters for two kinds of performances are presented in Table 6. Regardless of the installed BL bleed system, the area of the low-pressure zone at the edge of the outlet section effectively decreased. In addition, the positive phenomenon where the low-pressure zone was mainly distributed in the center of the outlet still existed, which conformed to the theoretical law. Therefore, the DC60 values of the three intakes were reduced by different degrees, but the flow coefficients and TPR coefficients were reduced as a cost. Comparison of the results of models D-1 and D-2 showed that the system at the concave side of the S-bend plays a positive role in improving the aerodynamic performance, while that on the other side plays a negative role, with the high-pressure flow bleeding out from the mainstream. The same conclusion can also be drawn from the total pressure and mass flow of the outlet. Although the outlet area of model D-1 was twice that of model D-2, the mass flow of model D-1 was more than twice that of model D-2,

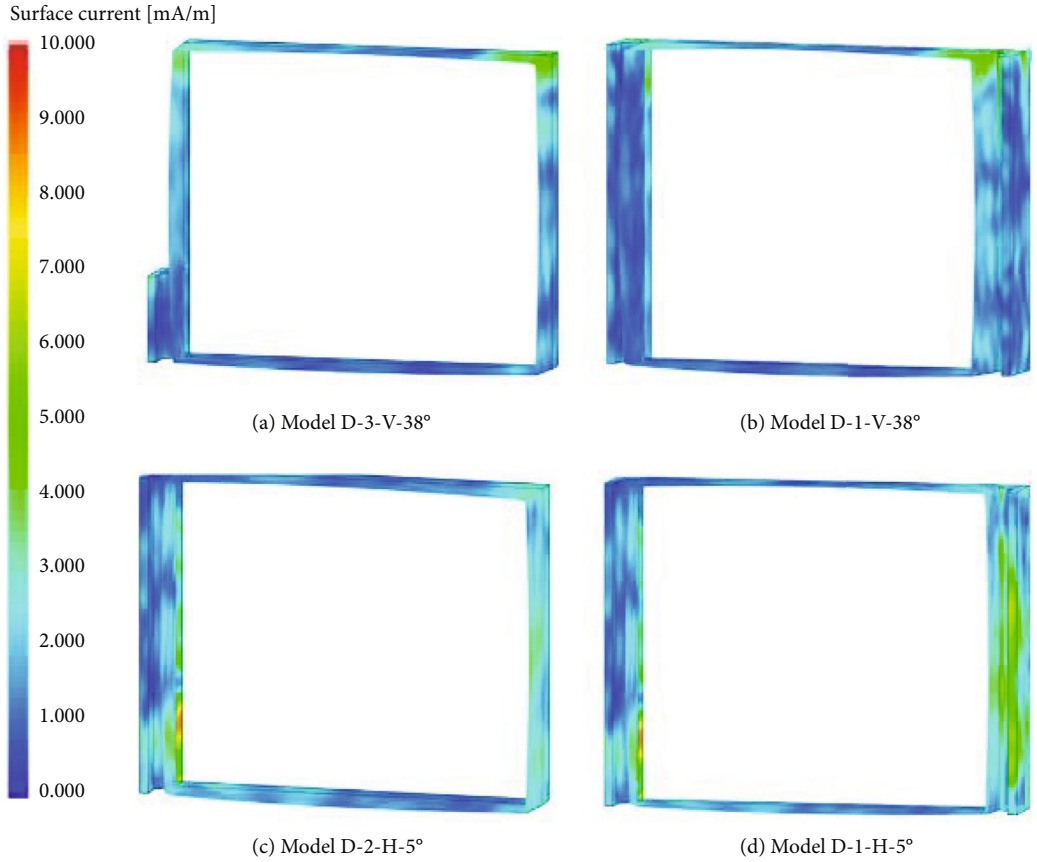

Figure 20: Surface current distribution of the different boundary-layer bleed systems.

and the average total pressure values of the two models were also obviously different, signifying that part of the mainstream bled out from the outlet of model D-1. Therefore, for the S-duct diffuser with an uneven flow field distribution, the traditional symmetrical installation scheme of a boundary-layer bleed system is inapplicable.

In terms of electromagnetic scattering, the boundary-layer bleed system had different effects on the performance of the intake radiated by two different polarized waves due to the different sizes. When the incident wave was vertically polarized, the average RCS values of all the intakes increased and SA decreased; i.e., the performance deteriorated. When the incident wave was horizontally polarized, the outcome was reversed, although the performance change was less significant. The results of the electromagnetic scattering calculations are presented in Figure 19. Regardless of the installed boundary-layer bleed system, the variation and the RCS values exhibited no significant change when the incident wave was horizontally polarized. When the incident wave was vertically polarized, only the RCS variation of model D-3 was consistent with that of model D. The RCS values of models D-1 and D-2 were significantly different from those of model D with incident angles of 30°–45°.

Figure 20 presents the partial section current distribution of different boundary-layer bleed systems. Figure 20(a) shows the current distribution of model D-3 radiated by a vertically polarized wave with an incident angle of 38°. The currents of the system in model D-3 were at a low level, even less than those of the nearby diffuser surface. Multiple large-current zones appeared on the right and upper-left surfaces of the systems in model D-1, as shown in Figure 20(b). Therefore, the difference between the RCS values of models D-1 and D was larger than that of models D-3 and D in this condition. Moreover, the currents of the diffuser surface near the system on the concave side of model D-1 were smaller than those of model D-3, proving that the cavity structure of the boundary-layer bleed system changed the original path of the electromagnetic wave. This phenomenon also played a positive role with some incident angles. Similarly, multiple large-current zones appeared on the system at the convex side of the diffuser irradiated by the horizontally polarized wave with an incident angle of 5°, which increased the RCS value.

In summary, when installing a boundary-layer bleed system in the right position, the aerodynamic performance of an intake can be improved while reducing the loss of electromagnetic scattering performance. Furthermore, when determining the appropriate structural parameters, the installation of the boundary-layer bleed system plays a positive role on the aerodynamic and electromagnetic performances of the intake.

4. Conclusions

(1) The phase angle change of the compressor rotor blade can lead to obvious differences in the RCS values of a caret intake with the same incidence angle

as the electromagnetic wave. Compared to a straight intake, the S-duct diffuser can effectively suppress this phenomenon in an S-duct intake, with an average RCS decrease of 7.65 dB and the decrease of the maximum RCS difference caused by the blade rotation of 6.75 dB. However, as a cost, the TPR coefficient of the S-duct intake decreases by 0.004, and the flow coefficient decreases by 0.003 with the critical pressure decreasing to 60,000 Pa

(2) Multiple boundary-layer separations and backflows occur in the diffuser of a traditional S-duct caret intake, resulting in the loss of the flow capacity. A double S-duct intake can effectively suppress these phenomena by changing the shape of the centerline. Moreover, compared to a straight intake, a double S-duct intake can more fully shield the outlet and increase the consumption of the electromagnetic wave in the cavity, resulting in the reduction of the RCS value. Compared to a traditional S-duct intake, for the proposed intake with suitable model parameters, the average RCS value was lower by 0.05 dB, and the TPD was lower by 0.18

(3) Due to the extremely uneven flow distribution in the diffuser of a double S-duct intake, the traditional symmetrical boundary-layer bleed system can easily result in the outflow of the mainstream. In addition, as a cavity, the boundary-layer bleed system leads to the change of the surface current and increase of the RCS value. To simultaneously resolve both these issues, a unilateral partial bleed system was designed that decreased the TPD by 0.04 and increased the average RCS value by −2.17 dB, compared to an intake without the bleed system

(4) Based on the above conclusions, the wall configuration of an S-duct diffuser considerably influences the aerodynamic and electromagnetic performances of an intake. Therefore, an optimal diffuser design could be an effective way for improving the aerodynamic and electromagnetic performances. However, considering the long length of time required for the numerical calculation of each intake, a high-precision proxy model needs to be established to improve the optimization efficiency

Data Availability

There is no data availability statement to declare.

Conflicts of Interest

The authors declare that they have no conflicts of interest.

References

[1] C. S. Lee, S. W. Lee, and R. Chou, "RCS reduction of a cylindrical cavity by dielectric coating," in *Proceedings of the IEEE International Symposium on Antennas and Propagation Digest, Volume 1*, pp. 305–308, Philadelphia, PA, USA, 1986.

[2] G. R. Hall, W. M. Hurwitz, G. S. Tiebens, W. P. Norby, P. Singshinsuk, and C. E. Wilt, "Development of the F/A-18E/F air induction system," in *AIAA*, pp. 93–2152, Reston, VA, USA, 1993.

[3] J. Syberg, J. Koncsek, and L. Surber, "Performance variations in high aspect ratio subsonic diffusers due to geometric constraints in supersonic tactical aircraft inlet installations," in *Proceedings of the AIAA/SAE/ASME 16th Joint Propulsion Conference*, Hartford, CN, USA, 1980.

[4] B. H. Little and W. S. Trimbol, "An experimental investigation of S-duct diffusers for high-speed prop-Fans," in *Proceedings of the AIAA/SAE/ASME 18th Joint Propulsion Conference*, Cleveland, OH, USA, 1982.

[5] W. H. Ball, "Experimental investigation of the effects of wall suction and blowing on the performance of highly offset diffusers," in *Proceedings of the AIAA/SAE/ASME 19th Joint Propulsion Conference*, Seattle, Washington, USA, 1983.

[6] R. A. Kitchen and D. Sedlock, "Subsonic diffuser development of advanced tactical aircraft," in *Proceedings of the AIAA/SAE/ASME 19th Joint Propulsion Conference*, Seattle, Washington, USA, 1983.

[7] P. D. Bravo-Mosquera, A. M. Abdalla, H. D. Cerón-Muñoz, and F. Martini Catalano, "Integration assessment of conceptual design and intake aerodynamics of a non-conventional air-to-ground fighter aircraft," *Aerospace Science and Technology*, vol. 86, pp. 497–519, 2019.

[8] D. Chaussee and T. H. Pulliam, "A diagonal form of an implicit approximate-factorization algorithm with application to a two dimensional inlet," in *Proceedings of the 18th Aerospace Sciences Meeting*, Pasadena, CA, USA, 1980.

[9] C. Fiola and R. K. Agarwal, "Simulation of secondary and separated flow in a diffusing S-duct using four different turbulence models," *Aerospace Engineering*, vol. 228, no. 11, pp. 1954–1963, 2014.

[10] S. Jeyatharsan, A. Cristhian, and S. John, "Numerical simulation of an aircraft engine intake S-duct diffuser," in *53rd AIAA/SAE/ASEE Joint Propulsion Conference*, Atlanta, GA, USA, 2017.

[11] B. J. Connolly, E. Loth, and C. Frederic Smith, "Unsteady separated flows in an S-duct and a bifurcating duct," *Journal of Aircraft*, vol. 59, no. 1, pp. 47–57, 2022.

[12] G. Wenbiao and Z. Xiaocui, "Design optimization of a three-dimensional diffusing S-duct using a modified SST turbulent model," *Aerospace Science and Technology*, vol. 63, pp. 63–72, 2017.

[13] J. W. Crispin Jr. and A. L. Maffett, "Estimating the radar cross section of a cavity," *IEEE Transactions on Aerospace and Electronic Systems*, vol. 6, pp. 672–674, 1970.

[14] K. Umashankar, A. Taflove, and S. Rao, "Electromagnetic scattering by arbitrary shaped three-dimensional homogeneous lossy dielectric objects," *IEEE Transactions on Antennas and Propagation*, vol. 34, no. 6, pp. 758–766, 1986.

[15] S. S. M. Chung and S.-C. Tuan, "Efficacy of an S-shaped air inlet on the reduction of front bistatic radar cross section of a fighter engine," *Progress in Electromagnetics Research B*, vol. 92, pp. 193–211, 2021.

[16] J. Lee, S. Lee, and J. Cho, "Effect of inlet boundary layer suction on flow distortion in subsonic diffusing S-duct," *International Journal of Aeronautical and Space Sciences*, vol. 20, no. 4, pp. 850–857, 2019.

[17] G. McLelland, D. G. Mac Manus, P. K. Zachos, D. Gil-Prieto, and M. Migliorini, "Influence of upstream total pressure profiles on S-duct intake flow distortion," *Journal of Propulsion and Power*, vol. 36, no. 3, pp. 346–356, 2020.

[18] S. P. S. Pattnaik and N. K. S. Rajan, "Numerical investigation of impact of fixed-exit boundary-layer bleed on supersonic intake performance," *Aerospace Science and Technology*, vol. 120, article 107286, 2022.

[19] H. Wei, W. Han, Y. Yan-guang, and Y. Li, "Recent advances in the shock wave/boundary layer interaction and its control in internal and external flows," *Acta Astronautica*, vol. 174, pp. 103–122, 2020.

[20] D. Zhao-bo, S. Chi-bing, S. Yang, H. Wei, and Y. Li, "Design exploration on the shock wave/turbulence boundary layer control induced by the secondary recirculation jet," *Acta Astronautica*, vol. 181, pp. 468–481, 2021.

[21] Z. B. Du, C. B. Shen, W. Huang, Y. Shen, H. Wu, and Y. Han, "Investigation on the three-dimensional shock wave/turbulence boundary layer control induced by the secondary recirculation jets," *Computers & Fluids*, vol. 237, article 105341, 2022.

[22] X. Y. Zhong, W. Huang, L. Yan, H. Wu, and Z. B. Du, "Investigation on the adaptive control of shock wave/turbulent boundary layer interaction based on the secondary circulation jets," *Acta Astronautica*, vol. 198, pp. 233–250, 2022.

[23] H. Wu, W. Huang, L. Yan, and Z. B. Du, "Control mechanism of micro vortex generator and secondary recirculation jet combination in the shock wave/boundary layer interaction," *Acta Astronautica*, vol. 200, pp. 56–76, 2022.

[24] W. H. Choi, T. I. Kim, and W. J. Lee, "Broadband radar absorbing sandwich composite with stable absorption performance for oblique incidence and its application to an engine duct for RCS reduction," *Advanced Composite Materials*, vol. 30, no. 1, pp. 76–90, 2021.

[25] B. Wang and Q. Wang, "Numerical optimization of electromagnetic performance and aerodynamic performance for subsonic S-duct intake," *Aerospace*, vol. 9, no. 11, p. 665, 2022.

[26] R. R. Zhang, W. Huang, L. Q. Li, L. Yan, and R. Moradi, "Drag and heat flux reduction induced by the pulsed counterflowing jet with different periods on a blunt body in supersonic flows," *International Journal of Heat and Mass Transfer*, vol. 127, pp. 503–512, 2018.

[27] M. Ou, L. Yan, W. Huang, S. B. Li, and L. Q. Li, "Detailed parametric investigations on drag and heat flux reduction induced by a combinational spike and opposing jet concept in hypersonic flows," *International Journal of Heat and Mass Transfer*, vol. 126, pp. 10–31, 2018.

[28] C. D. Herrmann and W. W. Koschel, "Experimental investigation of the internal compression of a hyper-sonic intake," in *Proceedings of the 38th AIAA/ASME/SAE/ASEE Joint Propulsion Conference & Exhibit*, Indianapolis, Indiana, 2002.

[29] H. T. Anastassiu, J. L. Volakis, and D. C. Ross, "The mode matching technique for electromagnetic scattering by cylindrical waveguides with canonical terminations," *Journal of Electromagnetic Waves and Applications*, vol. 9, no. 11-12, pp. 1363–1391, 1995.